

Significance of third body rheology in friction at a dry sliding interface observed by a multibody meshfree model: Influence of cohesion between particles

Yinyin Zhang, Guilhem Mollon, Sylvie Descartes^{*}

Univ Lyon, INSA-Lyon, CNRS UMR5259, LaMCoS, F-69621, France

ARTICLE INFO

Keywords:

Multibody meshfree model
Third body rheology
Cohesion strength
Activated third-body thickness (ATT)

ABSTRACT

The third body approach deals with friction as a problem of third body rheology. Using a multibody meshfree model, we report influence of cohesion on third body rheology and friction at a dry sliding contact. With cohesion increasing from 0.0001 to 20 GPa, friction firstly increases linearly then transitions to a constant value, based on which three friction regimes are identified. Low cohesion (0.0001–1 GPa) is featured by lamellar flow; medium cohesion (1–5 GPa) triggers formation of strong inclined force chains; high cohesion (5–20 GPa) results in generation and rolling of agglomerates. How third bodies accommodate velocity gradient and transfer load are carefully examined. The results provide a possible novel approach of material design to monitor the coefficient of friction.

1. Introduction

A better understanding and control of friction in engineering contacting surfaces are gaining increasing attention as scientists and engineers have realized that a focus on tribology could provide “breathing space” while comprehensive solutions to environmental and energy problems are being addressed [1]. The third-body approach, a mechanical view of tribology, was introduced into dry sliding conditions by Godet et al., in 1980s and it brought the understanding of friction from volume that focused on the measurable material properties of first bodies yet ignored friction mechanisms, to interfaces that concentrated on the role of third bodies [2–4]. It deals with friction as a problem of third body rheology [4–6]. Experimental evidence, in particular from in situ techniques, has demonstrated that friction change is directly correlated to third body processes that include thickening, thinning, shearing, and loss of transfer films, generation and ejection of wear debris and sliding-induced mechanical and chemical changes [3,7–11]. Combining a tribometer with optical microscopy and Raman spectroscopy, Singer et al. [3] reported formation of stationary transfer films on the counterfaces during sliding of Pb–Mo–S and diamond-like carbon (DLC) coatings against transparent hemispheres; that resulted in interfacial sliding between the transfer films and the wear tracks, which gave rise to low and stable frictions running in dry air. Scharf et al. [11]

observed how friction was controlled by third body behaviour during running-in of titanium- and tungsten-doped DLC coatings sliding against sapphire. The friction of tungsten-doped DLC at the first ~30 cycles was high (~0.6) due to lack of transfer film, then decreased rapidly because of accumulation of transfer film, during which shearing and extrusion of third body material played an important role, and finally stabilized at ~0.07 when stationary transfer film was formed [11]. Titanium-doped DLC, however, yielded immediate reduction in friction to ~0.06 during the initial 10 cycles as a result of generation of transfer film, and continuous thickening of the transfer film further decreased friction to ~0.04 [11]. More recent work on metallic materials, i.e. aluminium sliding against sapphire, presented that frequent detachment and formation of transfer films in the contact contributed to fluctuating friction [12].

Even so, in situ techniques encounter three major challenges for probing third body behaviours in a constrained contact and their relationship with friction. First, it is impossible to explore influence of a single parameter without changing the others [13]. For instance, third body behaviour is highly related to local stress and third body properties including morphology, physicochemical and mechanical properties; one can easily vary the local stress by adjusting normal force, yet that leads to changes in third body properties as well [13]. Second, the transparent counterfaces often have very different mechanical and physicochemical

^{*} Corresponding author.

E-mail address: sylvie.descartes@insa-lyon.fr (S. Descartes).

properties from those commonly used in industry. Finally, in situ techniques nowadays are not capable of capturing third body processes such as their velocity, stress, strain and local arrangement. Therefore, numerical models are required to provide a fundamental understanding of third body rheology and its relation to friction for a dry sliding contact. The most frequently used approach to model third body rheology is discrete element modelling (DEM) that was developed by Cundall and Strack in 1979 for granular materials [14]. Third bodies were described as assemblies of rigid spheres between two parallel surfaces in shearing [15–20]. Early work by Iordanoff et al. [18,19] examined influence of cohesion on third body dynamics in both two- and three-dimension forms. Similarly, using two- and three-dimensional models, Fillot et al. [15,16] implemented degradable first body into the discrete element model and established an early wear model. Mollon [21] later introduced surface roughness of first bodies into the 3D model. More recent models often combined discrete element model and finite element model (DEM + FEM), in which the third bodies were seen as discrete elements while the first bodies were modelled by finite elements [17,20,22]. This approach enabled to calculate deformation in the first bodies, as well as interactions between first and third bodies.

Even though the above models contribute to a significant progress of better understanding third body processes in a constrained contact, none of them takes into account deformability of third bodies. This raises questions when reproducing tribological contacts where metallic materials are involved. Experimental studies display abundant evidence of large plastic deformations in third bodies which play a crucial role in evolution of third body properties such as morphology, microstructure and mechanical property [23,24]. Therefore, a Multibody Element-free Open code for Dynamic simulation (i.e. MELODY) was proposed by Mollon and focused on simulations of deformable granular materials under shearing [25,26]. This framework combined advantages from both continuous modelling in which stress and strain inside the particles can be extracted, and discontinuous methods that were capable of analysing interactions of a large number of particles. Hence, it became a useful tool to study third body rheology in a sliding contact [27].

In the present work, MELODY was applied to examine how third body rheology affects friction behaviour in a dry sliding contact. With varying cohesion between third body particles, focus was placed on the following research questions: How do the third bodies flow in the contact? How do the third bodies accommodate velocity gradient of the two first bodies? How do the third bodies transmit load? In addition, third body characteristics and friction behaviour of a steel/steel contact were observed experimentally in a fretting scenario to provide empirical evidence to the numerical model.

2. Methodology

2.1. Multibody meshfree modelling

Fig. 1a exhibits an illustrative view of the code MELODY applied to

the current study, which comprises two flat rigid first bodies in parallel. Their length is $\sim 20 \mu\text{m}$ that depicts the microscale nature of the present modelling. There are 192 deformable third body particles under compression with a constant normal pressure of 1 GPa that is imposed onto the upper border of the upper first body. Circles and ellipses are used to describe various third body morphologies that have been widely observed experimentally [12,28,29]. Zhang et al. [29] documented that in a fretting contact of copper matrix composites (i.e. Cu + MoS₂ and Cu + MoS₂+WC) sliding against stainless steel, third body morphology and size changed with cycle numbers and one contact often contained third bodies with various morphologies and sizes. During the steady-state, flake-like wear debris ranged from $\sim 0.5 \mu\text{m}$ to several micrometres in size [29]. Therefore, diameters of the circles in the present simulation were set as 0.3–0.5 μm ; while the ellipses held short axes of 0.6–1.2 μm , and long axes of 1–2 μm , resulting in ellipses roughly 5 times larger than the circles. The mix contains the same number of circles and ellipses, i.e. 96, whose density was set as 6.4 g/cm³ to represent iron oxides. This is to match our experimental setup where a self-mated contact of steel 35NCD16 was examined.

Young's modulus and Poisson ratio of the third body particles were set as 10 GPa and 0.45, respectively. It is important to note that those two parameters in MELODY are measures of deformability and compressibility of the third body particles, respectively, and they are phenomenological values. After many tests on various values, the above setup not only permitted a robust model capable of varying cohesion and particle sizes in a wide range, but also led to third body behaviors that were reasonable from an empirical point of view. The study on particle sizes will be presented in a future publication. Another important reason why those phenomenological values were applied is that experimental measurements of third bodies under real tribological conditions is still a big challenge, hence no reliable data base is available at the moment.

A lateral velocity of 100 m/s was imposed to the upper first body to initiate relative shearing between the two first bodies. One may notice a large difference in the sliding velocity values of macroscale experimental setup ($\ll 1 \text{ m/s}$) compared to the present microscale simulations [30]. First, at the lower sliding speeds, the experiments can observe dynamics of a larger scale sliding contact. Although with different sliding velocities, the microscale response can be similar because the simulations reach steady-state within a much shorter time scale ($\sim 0.5 \mu\text{s}$). Moreover, such a high speed turned out to be necessary because of the explicit solver used in MELODY, as was seen in molecular dynamics simulations [31]. Besides, the shearing speed in our simulation is within the operating velocities of high speed electrical contacts that can reach 75 m/s [32], thus it is relevant. Periodic boundary conditions were applied to the model and the total sliding distance of each simulation was 400–450 μm that permitted a long statistically meaningful stable-state of $\sim 400 \mu\text{m}$.

As seen in Fig. 1b, unlike finite element modelling, the third body particles are described using field nodes that are distributed in particle interior and contact nodes that are located at particle boundaries. Each

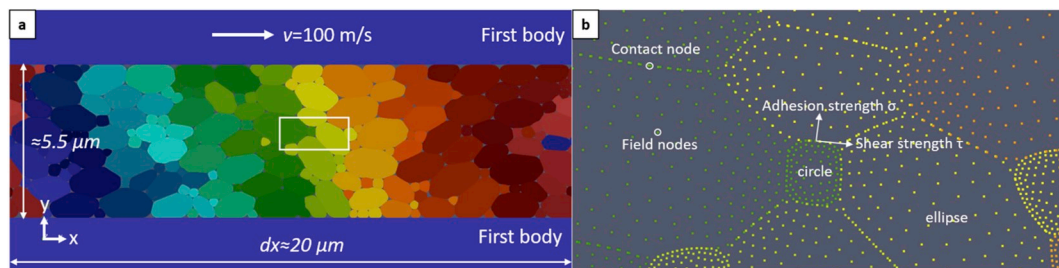


Fig. 1. (a) Multibody meshfree model that depicts cross-sectional view of two rigid first bodies under compression with deformable third bodies in between (arbitrary colors); (b) a close view of the rectangle in (a), exhibiting distribution of nodes in the particle interior (field nodes) and edge (contact nodes), as well as definition of shear strength (τ) and adhesion strength (σ) between particles. (For interpretation of the references to color in this figure legend, the reader is referred to the Web version of this article.)

node has two degrees of freedom (i.e. X and Y axes), which contribute to motion of the third body particles constrained to cross-sectional view (see Fig. 1a). A continuous displacement field between two neighbouring nodes in the particle interior (including boundary) was interpolated by Moving Least Square (MLS) meshfree shape functions [33]. According to their strain fields, which was computed from displacement field, stress field was calculated by a weak formulation combined with a classical quadrature numerical integration. Importantly, the contact nodes and segments are also responsible for detection of particle interactions using a penalty-based two-ways contact algorithm. Therefore, spatial density of the nodes is the highest at the particle boundaries and reduced gradually towards the particle center (Fig. 1b). The lowest distance between two contact nodes for an ellipse is ~ 60 nm, while at the center it can be as great as ~ 170 nm; for the circles, the smallest distance between two contact nodes is ~ 30 nm, and the highest at center is ~ 90 nm. More fundamentals regarding particle interactions, specifically how non-linear equations were solved, and more applications can be found in previous work by Mollon [25,34].

In Fig. 1b, cohesion of two particles in contact is interpreted as shear strength τ , and adhesion strength σ . τ is defined as the shear force per unit area required to shear the interface, while σ is the tensile force per unit area required to pull apart the interface. For the sake of simplicity, identical values were assigned to shear strength and adhesion strength in this work, and they ranged from 0.0001 to 20 GPa for all interfaces among third body particles. Cohesion (τ and σ) between third bodies and the first bodies was set as 100 GPa in order to form a single layer of third bodies on the first bodies. Those layers could serve as interface between first body and third body, known as screens from experimental observations [35]. It is important to point out that cohesion values here are also phenomenological values that permit a robust model and, meanwhile, yield diverse scenarios of third body rheology which have been observed in experiments. Plus, experimental measurements of those values under a tribological condition are still difficult and will rely on future technology development. All the simulations were run on 20 processors on LaMCoS cluster.

2.2. Experimental

In order to provide experimental evidence to the present modelling, fretting tests that produced two types of third bodies with distinct cohesions were designed. A self-mated low alloy steel (35NCD16) with a tempered martensitic microstructure [36] was tested on a custom-built ball-on-plate fretting device (LaMCoS, INSA de Lyon, France) at room

temperature (20–25 °C). The upper ball had a radius of 100 mm, with a normal force of 80 N, creating a mean Hertzian contact pressure of ~ 200 MPa. The imposed slip amplitude was ± 120 μm , the oscillating frequency was 10 Hz, and the test duration was 10,000 cycles. The fretting tests were running in ambient air ($\sim 40\%$ relative humidity) and dry argon ($< 2\%$ relative humidity), respectively; we expected the former would generate oxidized third bodies that ought to exhibit low cohesion comparing to the latter case where metallic third bodies and adhesive wear would be dominant. The above running parameters were set up to achieve gross slip conditions. As shown in Fig. 2a, typical fretting loops during steady-state of both tests exhibit quasi-rectangular shapes, an indication of gross slip [37]. In Fig. 2b and c, fretting logs of the tests in air and in argon, respectively, indicate the tests entered steady-state after a short running-in period.

3. Results and discussion

In Fig. 3, the plot exhibits significant influence of cohesion strength between third body particles on friction evaluation. With increasing shear and adhesion strength (τ and σ), friction firstly rises to a peak value of ~ 0.69 at a cohesion strength of 3 GPa, then reduces slightly to ~ 0.64 at 5 GPa and eventually keeps constant with cohesion up to 20 GPa. Three friction regimes are assigned according to their responses to cohesion strength and they are referred to as linear, transition and constant friction regimes. At low cohesion (0.0001–1 GPa), friction increases linearly from ~ 0.14 to ~ 0.48 . Fluctuations of the friction values at this stage are generally low yet increase with cohesion. However, with further increase in cohesion (1–5 GPa), friction reaches a peak that appears ~ 0.69 at the cohesion of 3 GPa. Note that fluctuations of the friction are slightly higher than that during linear regime but keep constant when cohesion increases from 3 GPa to 5 GPa. At high cohesion strength (5–20 GPa), the average friction coefficients keep a rather constant average value at 0.58–0.62, but they fluctuate more and more with cohesion, leading to the greatest standard deviation of ~ 0.2 at the cohesion of 20 GPa. In the rest of this section, typical third body rheology in the three friction regimes are presented, based on which sliding mechanisms are revealed.

3.1. Linear friction regime at low cohesion (0.0001–1 GPa)

Cohesion strength of 0.0001 GPa and 1 GPa are selected as representatives in this friction regime. Fig. 4 depicts their typical von-Mises stress fields and corresponding normalized strain rate fields during

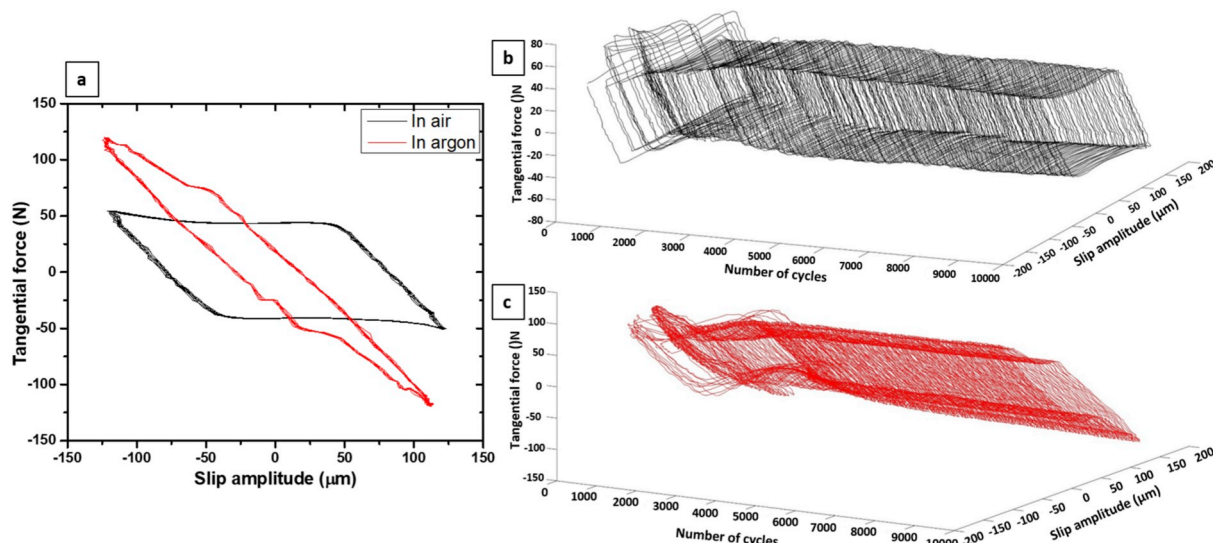


Fig. 2. (a) Typical fretting loops of the tests running in air and argon; (b) and (c) are their fretting logs.

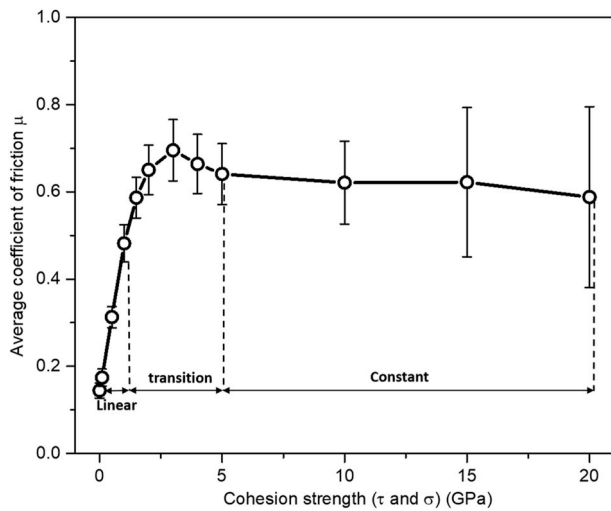


Fig. 3. Average coefficient of friction versus cohesion strength, in which three friction regimes are identified.

steady-state. Here, the normalized strain rate was calculated via increment in the norm of the Green-Lagrange strain tensor and it indicates where (inner- or inter-particles) in the third bodies the deformation is likely to occur [34]. It should be noted that there is one possible third body behaviour for the cohesion of 0.0001 GPa, yet two typical behaviours are featured the cohesion of 1 GPa. Examples at $t = 2.70 \times 10^{-7}$ s and $t = 2.05 \times 10^{-6}$ s are shown in Fig. 4. In all cases, the third body particles flow in a compact manner with a high packing fraction of 96%–98%. However, at 0.0001 GPa, the stress field is homogeneous without distinct stress concentration (Fig. 4a); while at 1 GPa, the third body particles start forming stress concentration patterns, shown as inclined chains at an angle of around 50° with the sliding direction (Fig. 4b and c). No detectable difference in VonMises stress distribution between the two third body behaviours at 1 GPa was found (Fig. 4b and c). Nevertheless, normalized strain rate fields show contrast between the three scenarios. At 0.0001 GPa, the strain rate field is homogenous and low (Fig. 4d). Nearly all the particles carry similar strain rate at the particle boundaries, indicating all particles shear with each other, by which the

velocity difference between the two first bodies is accommodated. Strain rate inside particles is negligible. However, when cohesion increases to 1 GPa, high strain-rate areas are formed. In Fig. 4e, several high strain-rate lines divide third body particles into several zones, inside which the strain rates are low. This suggests shearing mainly takes place through the high strain-rate lines, while the particles away from those lines have faint possibility to shear. The second possible flow pattern at 1 GPa is formation of a high strain-rate line that is parallel to the sliding direction (Fig. 4f). Therefore, third body particles are separated into layers and shear only occurs between those layers, yet the particles inside the layers show negligible relative motion with each other.

The third body rheology in this friction regime is further revealed by the velocity distributions. As shown in Fig. 5a and d, at cohesion strength of 0.0001 GPa, the third body particles flow between the two first bodies as a typical Couette flow, where their horizontal velocities increase linearly with a constant gradient from the bottom first body to the upper first body, and their vertical velocities are close to 0 m/s with a small expansion in the middle of the flow. At 1 GPa, however, large velocity gradients are developed roughly along the high strain-rate areas, leading to agglomerates that then flow at different speeds (Fig. 5b–c and e–f). Therefore, the velocity accommodation mode (VAM), a concept introduced by Berthier et al. [35] to describe how third body particles adapt velocity gradient in a tribological contact, is shearing between those agglomerates. Since the shearing paths are not necessarily parallel to the sliding direction (Fig. 5b), indicating there is vertical flow of third bodies, the particles show a more scattered distribution in the vertical velocities (Fig. 5e) comparing to that at lower cohesion strength (Fig. 5d). But when the particles shear through a single high strain-rate line, as seen in Fig. 5c and f, it exhibits as a well-developed lamellar flow, where the two layers carry disparate velocities along sliding direction, i.e. the upper layer flow at 90–100 m/s and the lower layer ~ 0 m/s, while the vertical velocities of the particles remain ~ 0 m/s. It is important to mark that in the lamellar flow, the particles are moving forward alternatively in the two forms that showing in Fig. 5e (also Fig. 4e) and Fig. 5f (also Fig. 4f). Therefore, the features such as high strain-rate lines (Fig. 4f) formed during the well-developed lamellar flow will rearrange to a rather random distribution (Fig. 4e) when the flow pattern switches from Fig. 5f to Fig. 5e.

Even though the above third body flows display different characteristics at cohesion of 0.0001 GPa and 1 GPa, the VAMs are basically the

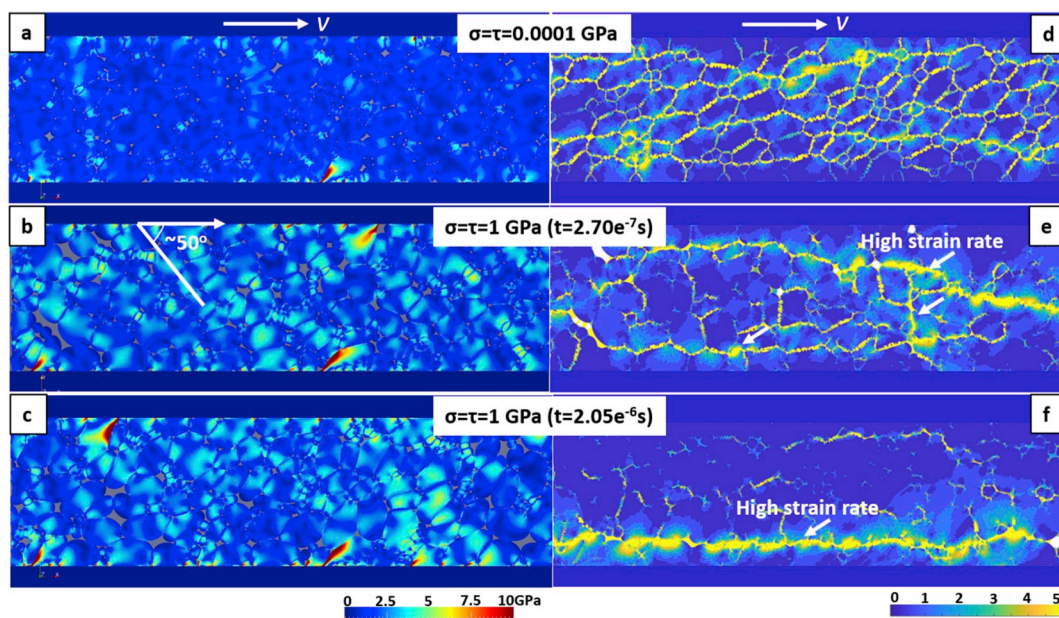


Fig. 4. Snapshots of von-Mises stress fields (a–c) and corresponding normalized strain rate fields (d–f) at cohesion strength of 0.0001 GPa and 1 GPa. Two typical third body behaviours are featured at 1 GPa cohesion. Arrows in (e) and (f) indicate high strain-rate areas.

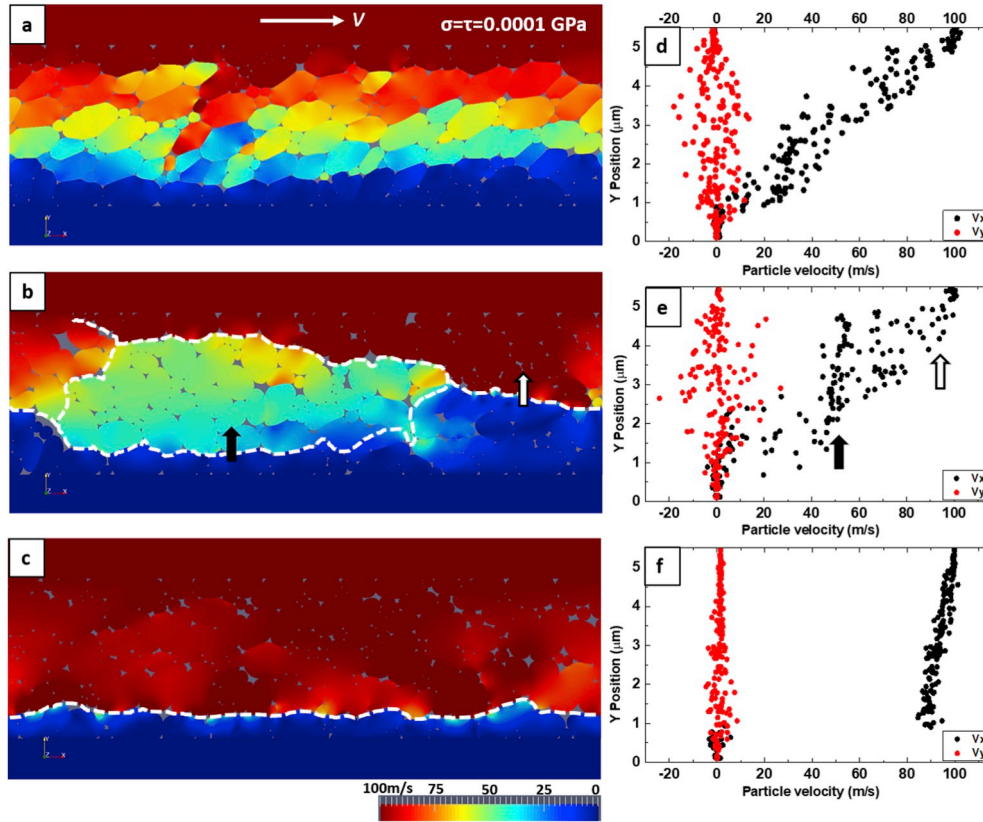


Fig. 5. Snapshots of typical velocity fields (a–c) and corresponding horizontal and vertical velocity profiles along the thickness of third body layer (d–f) at the cohesion strength of 0.0001 GPa and 1 GPa. The dashed lines in (b) and (c) indicate high velocity gradients; the arrows in (b) and (e) mark agglomerates flowing with different velocities.

same: shearing between the third bodies. In this case, friction is principally determined by shear strength. According to the classical theory of Bowden and Tabor on fundamentals of solid lubricants [38], the friction force, F , is a product of true contact area and shear strength of the contact, $A\tau$, friction can be expressed as $\mu = \frac{F}{L} = \frac{A\tau}{L} = \frac{\tau}{P_H} = \frac{\tau_0}{P_H} + \alpha$, where L is normal force, τ_0 is the interfacial shear strength, P_H is the mean Hertzian contact pressure, α is a constant that represents the lowest attainable coefficient of friction for a given friction couple. It is

apparent that when the mean Hertzian contact pressure keeps constant, the coefficient of friction increases linearly with the shear strength. Therefore, the third body rheology in this friction regime revealed from our simulations could be utilized to better understand the contact dynamics of solid lubricants where the dominant VAM is shearing between the third bodies.

Fig. 6 illustrates how third bodies transmit shear force and normal force during sliding. At 0.0001 GPa, the shear stress is low, less than 0.5

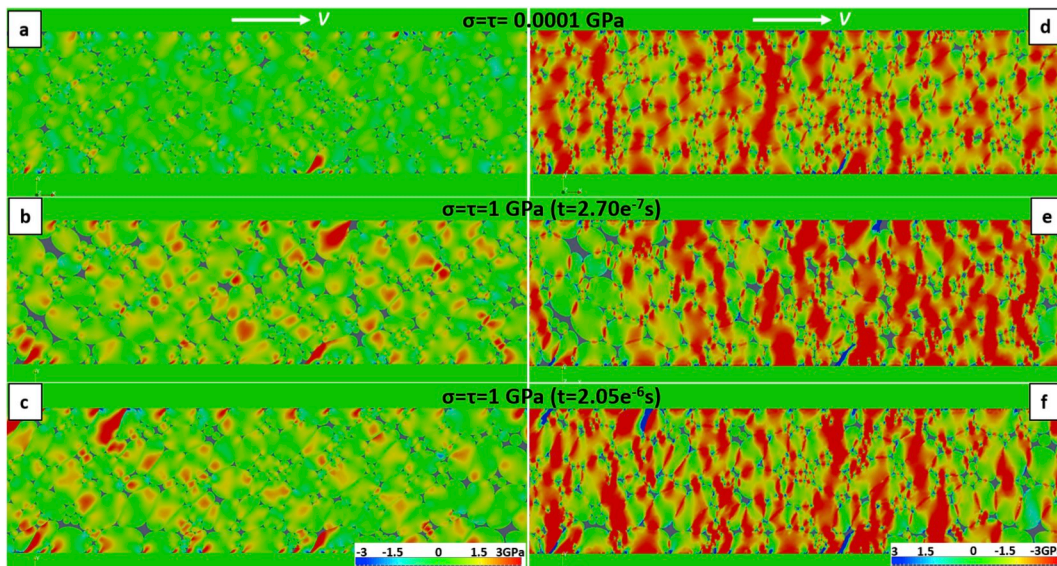


Fig. 6. Snapshots of typical shear stress fields (a–c) and vertical compressive stress fields (d–f) at cohesion of 0.0001 GPa and 1 GPa.

GPa, without noticeable stress concentration (Fig. 6a). When cohesion strength increases to 1 GPa, however, the shear stress is transmitted via stress concentration chains that are inclined 45° – 50° to the sliding direction (Fig. 6b). Those chains contain shear stress up to 1–2 GPa and the same pattern was found in the two typical third body behaviours at 1 GPa (Fig. 6c). As for the normal force, it is transmitted through stress concentration chains that are roughly perpendicular to the sliding direction and the stress magnitude of the chains is comparable, i.e. ~ 3 GPa, for cohesion strengths of 0.0001 GPa and 1 GPa (Fig. 6d–f). This could be due to the fact that the static particle arrangement in this friction regime is in a same manner (Fig. 6) and a constant normal pressure was applied. This suggests that load transmission via third body particles relied solely on static arrangement of the particles rather than third body dynamics.

3.2. Transition friction regime at medium cohesion (1–5 GPa)

In this friction regime, the highest friction at the cohesion strength of 3 GPa is selected to perform a closer observation on the third body behaviour. From Fig. 7a, the third body particles form strong inclined force chains with a packing fraction of $\sim 90\%$, lower than that in the linear friction regime (i.e. 96% – 98%). The inclined angle is generally not higher than 90° to the sliding direction. The third body particles deform moderately, particularly inside the force chains. It has been well documented in granular mechanics that existence of the force networks is a distinguishing feature of jamming state, in which the system can resist stresses without irreversible deformation [39,40]. Therefore, third body rheology through strong force chains gives rise to the highest coefficient friction. This scenario could be applied to interpret formation of “dense struts” or “prows” in sliding contacts of relatively soft metals such as titanium and aluminum [2,12]. Shockley et al. [12] observed gouged scars in the wear track caused by such “prows” that were adhered to the counterface.

Simulations reveal more details of those force chains. In Fig. 7b, high strain-rate areas mainly concentrate locally inside the chains and particle boundaries rather than particle interior. The velocity distribution (Fig. 7c and d) shows the particle speed decreases gradually from the upper to the lower first body, resulting in a constant and low velocity gradient along the sliding direction. That is similar to the Couette flow

observed in the linear friction regime (Fig. 5d), yet the vertical velocity distribution of the particles is more scattered, which is most likely due to frequent breakdown and regeneration of the force chains. Fig. 8 captures how one force chain evolves into two within a short time span of $1e^{-8}$ s. At $t = 1.139e^{-6}$ s (Fig. 8a), the particles inside the white rectangle are compacted in a thick force chain, it then splits into two at $t = 1.149e^{-6}$ s (Fig. 8b) via local slip inside the chain. Fig. 8c and d present local slip between particles and vertical velocities of the particles involved, respectively. The particles show low vertical velocities before and after slip, yet a high vertical velocity during the slip at $t = 1.145e^{-6}$ s. Interesting to note that the local slip occurs more and more frequently with cohesion strength in this friction regime, yet no direct relation was found between the number of such events and coefficient of friction.

Fig. 7e exhibits the shear force is transferred via the inclined force chains, in which stress concentration is ~ 3 GPa in magnitude, greater than that in the linear friction regime (Fig. 6). Normal force, nevertheless, is transmitted by vertical stress chains that hold a concentrated compressive stress of 4–6 GPa (Fig. 7f). The boost of shear stress with increased contact strength could be largely due to the raise in shear force; yet the increase in compressive stress primarily stems from the particle arrangement. Formation of the inclined force chains and reduction in the packing fraction lower the contact area of the first bodies and third bodies (excluding the layer stuck on the first bodies), and thus lead to a greater stress concentration inside the chains. As presented earlier, the “dense struts” and “prows” often stood out of the worn surface and they could be the real contacting points. Therefore, a high stress concentration was often created inside the “struts” and “prows” [12].

3.3. Constant friction regime at high cohesion (5–20 GPa)

Upon keep increasing cohesion strength, i.e. ≥ 5 GPa, the average friction coefficients stabilize at 0.58–0.62 (Fig. 3). This friction regime is characterized by large fluctuations in friction with time, evidenced by their increased standard deviations (Fig. 3). Therefore, 20 GPa is chosen to distinguish the features of third body rheology in this friction regime. Fig. 9a plots coefficient of friction versus sliding distance; it has a running-in peak during the first 12 μm , and then enters steady-state where the friction constantly fluctuates. Fig. 9b is a close view of a

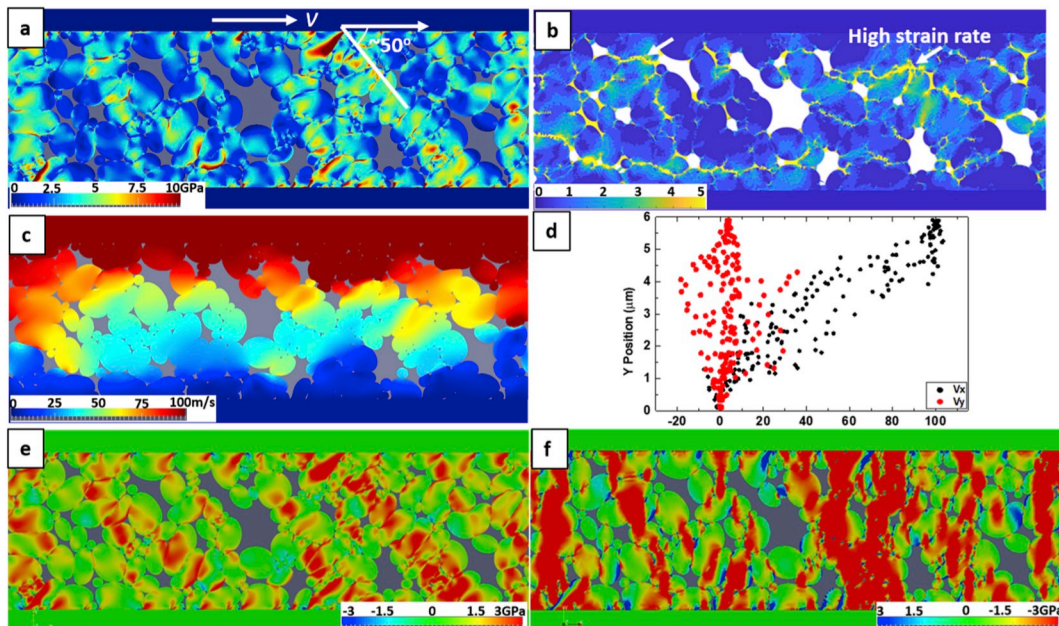


Fig. 7. (a) Snapshots of typical von-Mises stress field at 3 GPa, (b) corresponding normalized strain rate field, (c) velocity field, (d) horizontal and vertical velocity profiles along the thickness of third body layer, (e) shear stress field, and (f) vertical compressive stress field.

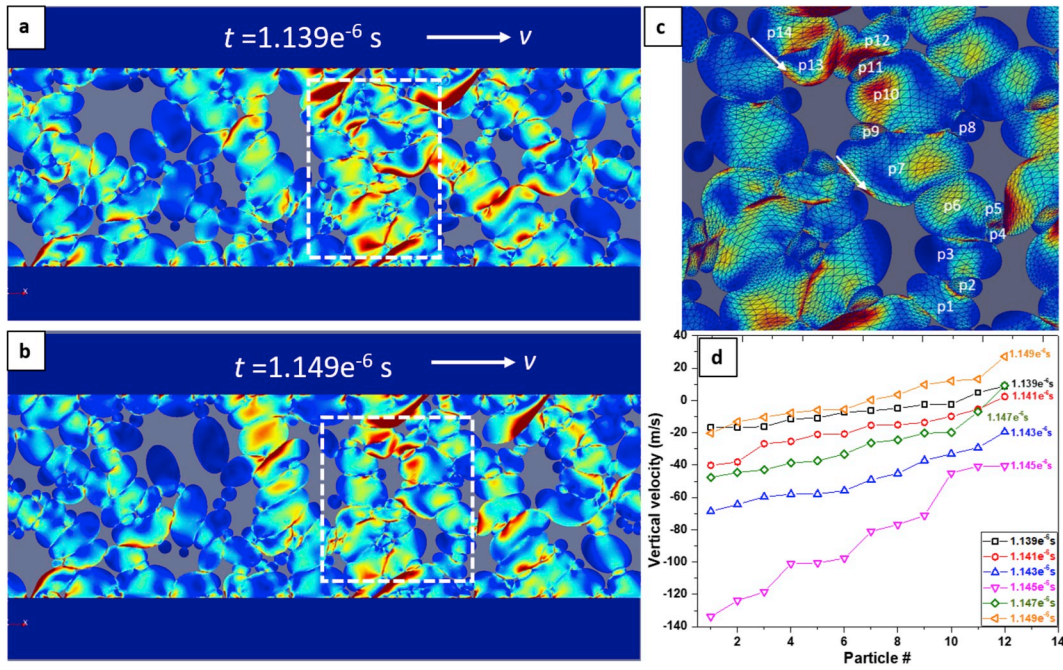


Fig. 8. Snapshots of Von Mises stress fields at 1.139×10^{-6} s (a) and 1.149×10^{-6} s (b). The rectangles indicate force chain evolution with time. (c) is a closer view of the rectangle in (b), indicating shear between particles. The involved particles are marked in (c). (d) is vertical profiles of those particles throughout the shearing event.

typical portion taken from Fig. 9a. Six snapshots taken from the moments labelled as #1 to #6 in Fig. 9b present their third body behaviours that yield various friction values. Generally, most third body particles undergo large deformations. At point #1, the particles start compacting, resulting in large pores in this layer and hence a low packing fraction of $\sim 80\%$. At point #2, when the friction is decreasing, majority of the particles compact together, forming a single large agglomerate. During point #2 and point #3, this agglomerate adapts the sliding by rolling,

with the particles in the upper part moving forward, yet the lower particles backwards, as indicated by the arrows in Fig. 9. At the moment of #4, large deformation takes place inside the agglomerate, contributing to friction increment. Subsequently, at #5, the agglomerate breaks down from interior and leads to a sudden drop in friction because such collapse releases the high cohesion between the particles. Finally, the third body particles flow as rather scattered particles without a special pattern and the friction keeps high, like that at moment #1.

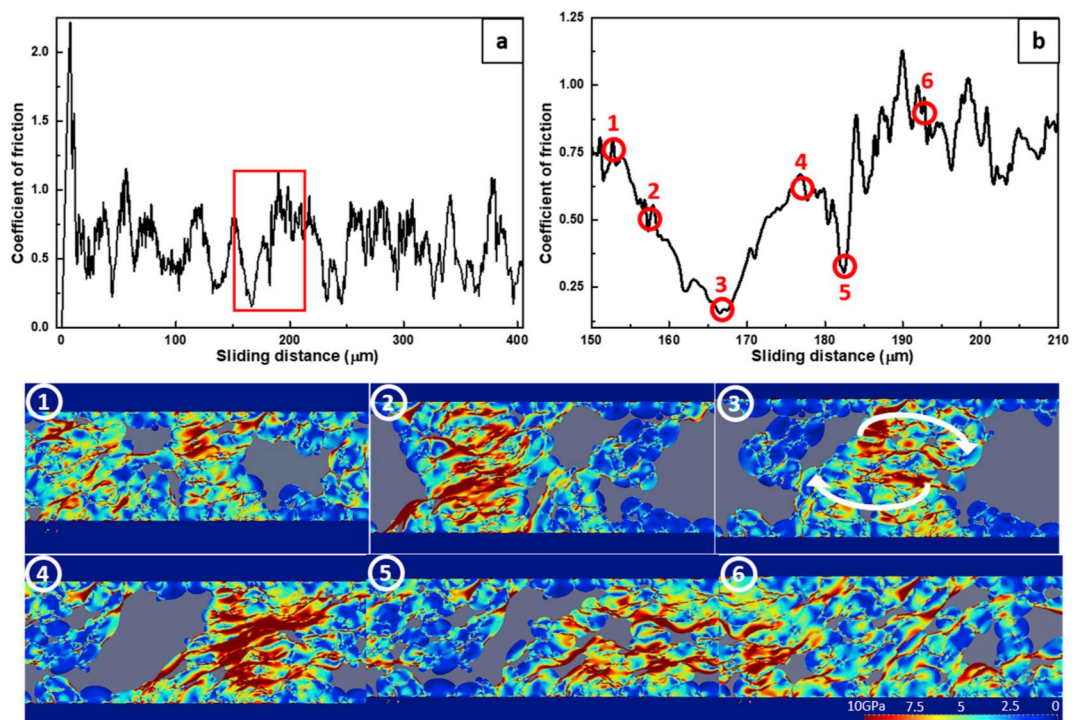


Fig. 9. (a) Plot of coefficient of friction versus sliding distance at a cohesion strength of 20 GPa; (b) a close view of the rectangle in (a); #1–#6 are snapshots of the von-Mises stress fields of third bodies at the moments indicated in (b). The white arrows in #3 mark flow directions of the particles.

It is evident that from #1 to #3, formation and rolling of agglomerates promote friction reduction. Experimental evidence of such velocity accommodation mode was provided in Berthier's early study where rolls were formed and adapted velocity difference in a fretting contact by rolling [41]. In addition, the friction drop at #5 induced by breakdown of cohesive third bodies was not only expected, but also found in experiment where adhesive wear was dominant. For example, during running-in period of a copper matrix composite fretting against steel, Zhang et al. [29] observed detachment of metallic agglomerates that occurred in adhesive zone. However, since those events were rather localized such that most of them did not easily correlate with friction change that was governed by numerous third body events across a whole contact area.

More features of the third body behaviour in this friction regime are revealed by the simulations. Fig. 10 presents normalized strain rate fields of the six moments in Fig. 9b. At point #1, high strain rate is concentrated at the edge of the agglomerate and roughly along the sliding direction (Fig. 10a). Shearing mostly occurs following the high strain-rate areas. Then during rolling of the agglomerate, high strain-rate is generated randomly depending on where deformation occurs (Fig. 10b&c). When the agglomerate undergoes severe deformation and eventually breaks down, a drastic strain rate concentration is created and, remarkably, in both particle interior and boundaries (Fig. 10d&e). In contrast to the linear and transition friction regimes where the third body particles flow via shearing through particle boundaries, severe deformation plays an important role when particles are strongly cohesive. In Fig. 10f, after the agglomerate breaks down, the high strain rate is concentrated along the sliding direction, similar to that at point #1 (Fig. 10a).

Characteristic velocity distributions and profiles of the particles are shown in Fig. 11. Before the agglomerate is formed, in Fig. 11a&a1, the particles flow with a rather constant and low velocity gradient along the sliding direction. Therefore, the velocity difference is adapted through a relatively thick layer. However, once the agglomerate is well developed and starts rolling, the velocity transition tends to concentrate in thin layers (Fig. 11b&c, 11b1&c1). Fig. 11d&e and d1&e1 indicate high

velocity gradients inside the agglomerate along the areas where it breaks down. When it is back to high friction, the velocity difference is accommodated in a thick layer, in which a low velocity gradient is generated (Fig. 11f & f1). Therefore, it is reasonable to state that high friction is associated with a thick transition layer to adapt the velocity difference, yet low friction correlates with a thin transition layer.

Fig. 12 exhibits how shear force and normal force are transferred via third bodies in the constant friction regime. In general, the shear force is transmitted via stress concentration chains that are 40–50° inclined to the sliding direction, which is similar to that in the linear and transition friction regimes (Fig. 12a–f). But during rolling and breakdown of the agglomerates (Fig. 12 c–e), such pattern is less distinguishable. The compressive force is transmitted by vertical stress chains throughout the whole process (Fig. 12 a1–f1). It is interesting to note that for the three friction regimes with cohesion ranging from 0.0001 GPa to 20 GPa, the stress chains formed in the third body layers often connect the two first bodies and almost all the third body particles are involved, therefore they activate the entire thickness of the third body layer to transfer shear and normal forces.

3.4. Activated third body thickness (ATT)

In Fig. 13a and b, we define arbitrarily the activated third body thickness (ATT) that is required to accommodate velocity difference as the third body layer in which particles carry velocities of 20–80 m/s. Those two values were selected based on the velocity distribution map (Fig. 13a). Following this concept, the mean ATT at various cohesion strengths were calculated by averaging the values throughout the steady-state (i.e. sliding distance from 50 to 400 μm) and plotted in Fig. 13c&d. In the linear friction regime (cohesion < 1 GPa), the ATT decreases with the cohesion, in contrast to the trend of the friction with cohesion strength. That gives rise to a reduction of friction with ATT (red points in Fig. 13d), suggesting that in this friction regime, friction is primarily depended on cohesion strength rather than the ATT. However, once enters the transition and constant friction regimes (cohesion \geq 1 GPa), the ATT and friction approximately follow the same trend;

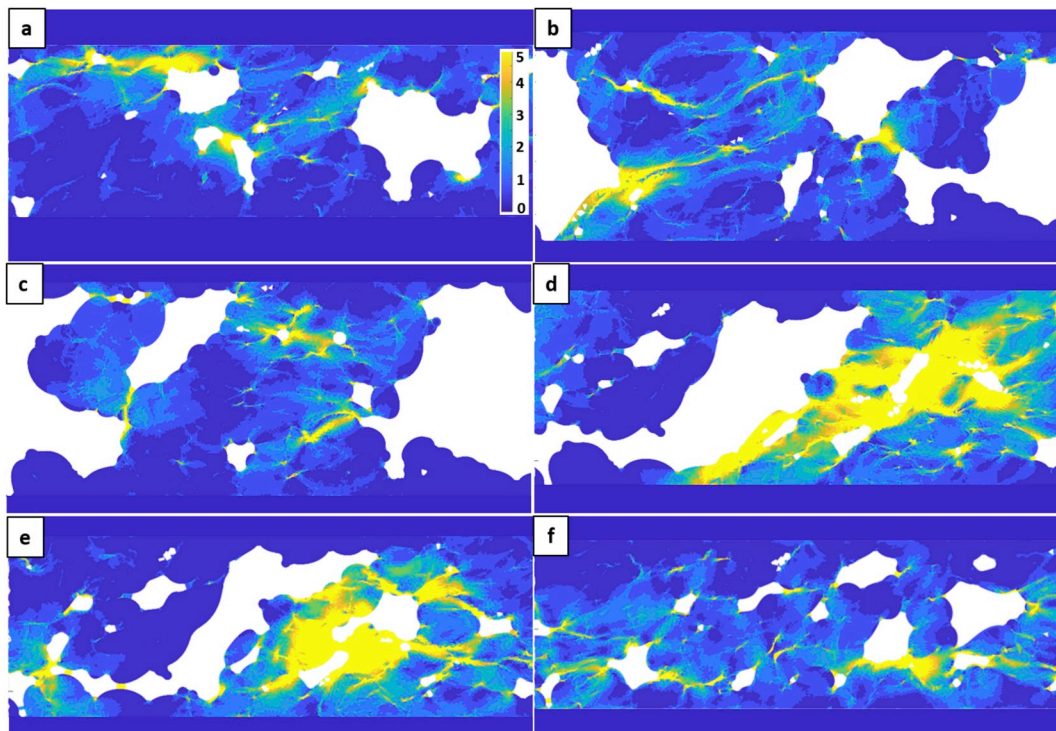


Fig. 10. Snapshots of normalized strain rate fields at the six moments marked in Fig. 9b.

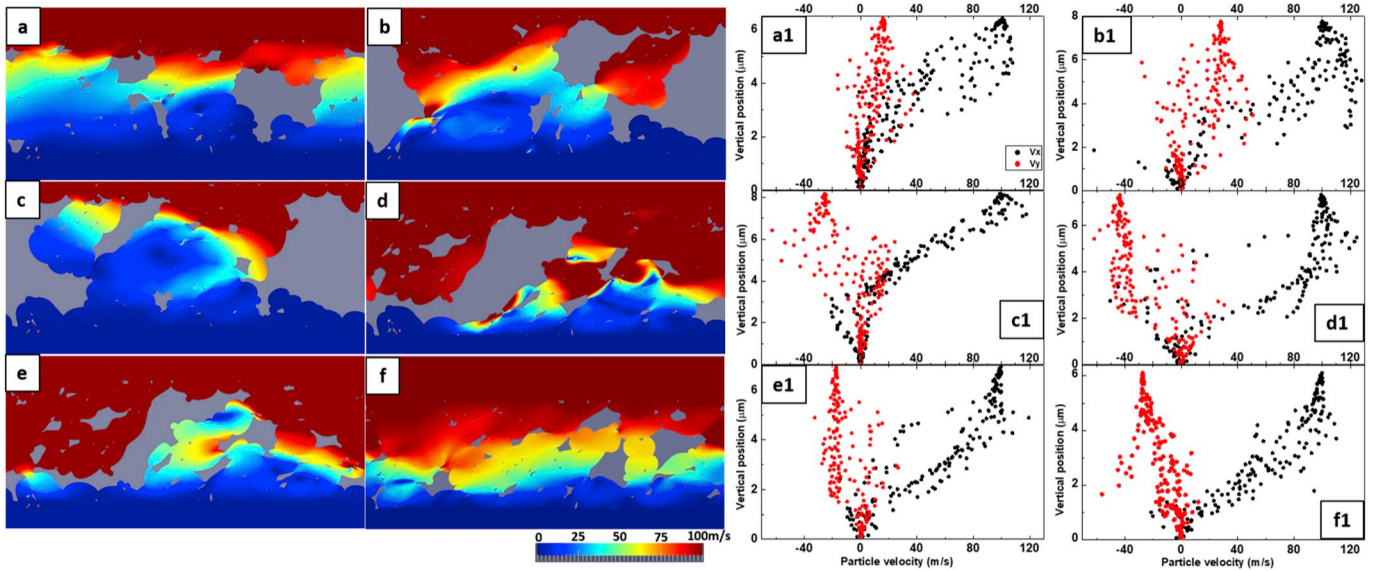


Fig. 11. Velocity fields and corresponding velocity profiles of third body particles at the six moments marked in Fig. 9b.

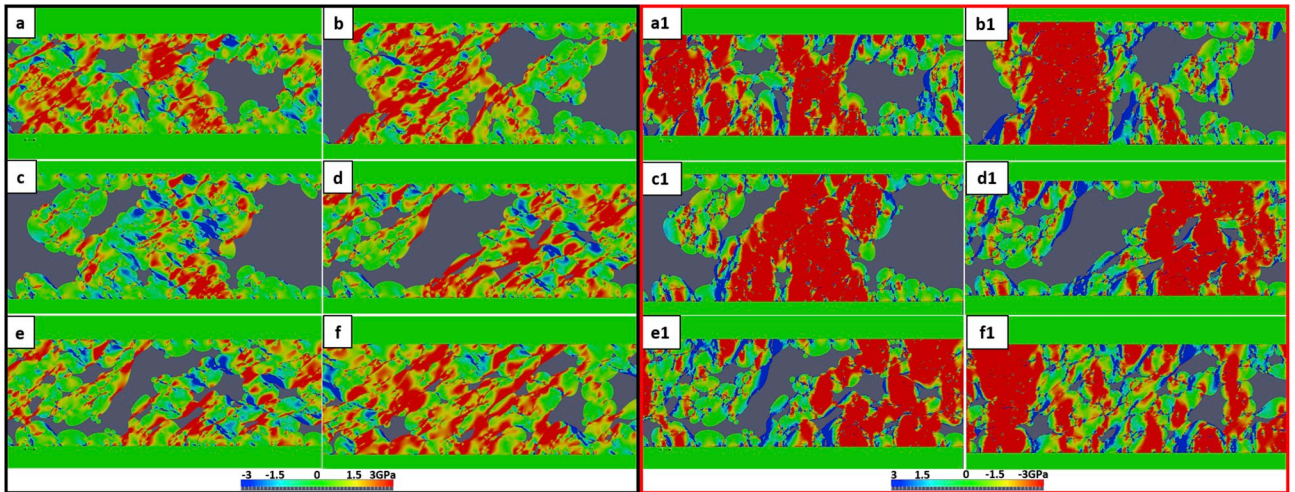


Fig. 12. Shear stress fields and vertical compressive stress fields of third body particles at the six moments marked in Fig. 9b.

therefore, coefficient of friction increases linearly with the ATT (black points in Fig. 13d). In other words, the thicker the third body layer that is required to accommodate the velocity difference, the higher the coefficient of friction. This statement links coefficient of friction directly and solely to the ATT, which holds only when the cohesion is medium and high (i.e. transition and constant friction regimes). This conclusion therefore provides a possible novel approach of material design to monitor the coefficient of friction. Further interpretation of the different responses of friction to the ATT in linear, transition and constant friction regimes is ongoing work and will be presented in the future.

Several questions regarding our model remain open and deserve discussion. The first concern is originated from the application of the Neo-Hookean constitutive model that uses elasticity to analyze materials behaviour subjected to large deformation, which has been commonly used for elastic materials such as rubbers [42]. Even though Neo-Hookean material probably could not fully replicate third bodies in a sliding contact, especially metallic materials as a sliding couple, the current simulation revealed instantaneous material response and showed increased deformation levels with cohesion (see Figs. 4 and 7&9). Moreover, although each particle behaved elastically, the whole layer exhibited an elastoplastic behaviour due to the irreversible relative

motion at the particle boundaries. That is a step forward comparing to conventional discrete element modelling, where all the particles were presumed to be perfectly rigid [16]. Second, utilization of phenomenological values in the model, e.g. Young's modulus and cohesion strength, although facilitated a robust model, led to weakness in physical meanings of the absolute values of stress and strain. Hence, the results here were only aiming to reveal their evolution with cohesion strength. Their physical meanings are still under investigation. Third, it is important to point out that the current version of MELODY concentrated on third body rheology during shearing at steady-state; its impact on the first bodies, that were set as rigid and nondegradable, was taken into account only through the frictional force produced at the first-body surfaces adjacent to the third bodies. Our future version (ongoing work) will extend to modification of the first-body microstructure and mechanical properties that are widely observed in tribology experiments [24], by implementing degradable first bodies. Eventually, influences of the first bodies to third body rheology and vice versa can be better understood. Finally, even though the current version of the code remains cross-sectional view (i.e. 2D), we believe the results obtained here can serve as a reasonable proxy for a 3D model. In fact, simulations of rigid granular materials showed that their typical behaviors, for instance

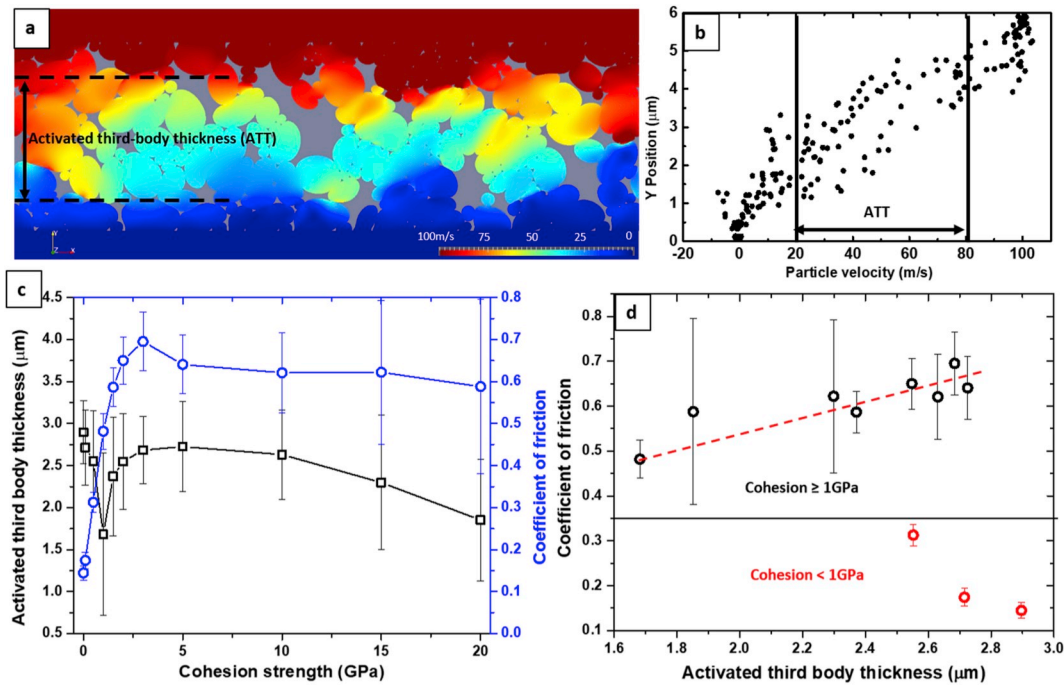


Fig. 13. (a) Activated third body thickness is defined from a velocity map and (b) from the velocity profile. (c) a plot of activated third body thickness and friction versus cohesion strength; (d) a plot of coefficient of friction vs. activated third body thickness.

force chains, dilatancy, and peak-plateau behaviour, etc. are probably better described and predicted in the 2D model [39,43]. A 3D model is theoretically doable, yet challenges reside in implementation and a substantial raise in computation cost.

3.5. Experimental results

Fretting tests running in air and argon exhibited distinct results. As shown in Fig. 14, the steady-state friction in air is 0.50 ± 0.01 , much lower than that in argon, i.e. 1.26 ± 0.01 . From Fig. 14b&c, the contacting surface after testing in air is fully covered by fine third body

particles and they are iron oxides (EDX not shown); the oxide layer is around 4–6 μm thick and the particles are rather loose. This implies cohesion between the particles is low. However, the sliding interface running in argon shows characteristics of adhesive wear, for instance, metal smearing and adhesive detachment (Fig. 14d). It is worth noting that no oxidation was detected by EDX on the wear track. Remarkably, large agglomerates with 10–30 μm in diameter are formed in the contact (Fig. 14e) and they are expected to roll according to their morphology. From cross section of the wear track (Fig. 14f), metallic third body particles are heavily deformed and compacted, forming dense agglomerate. That suggests strong cohesion between the third body particles.

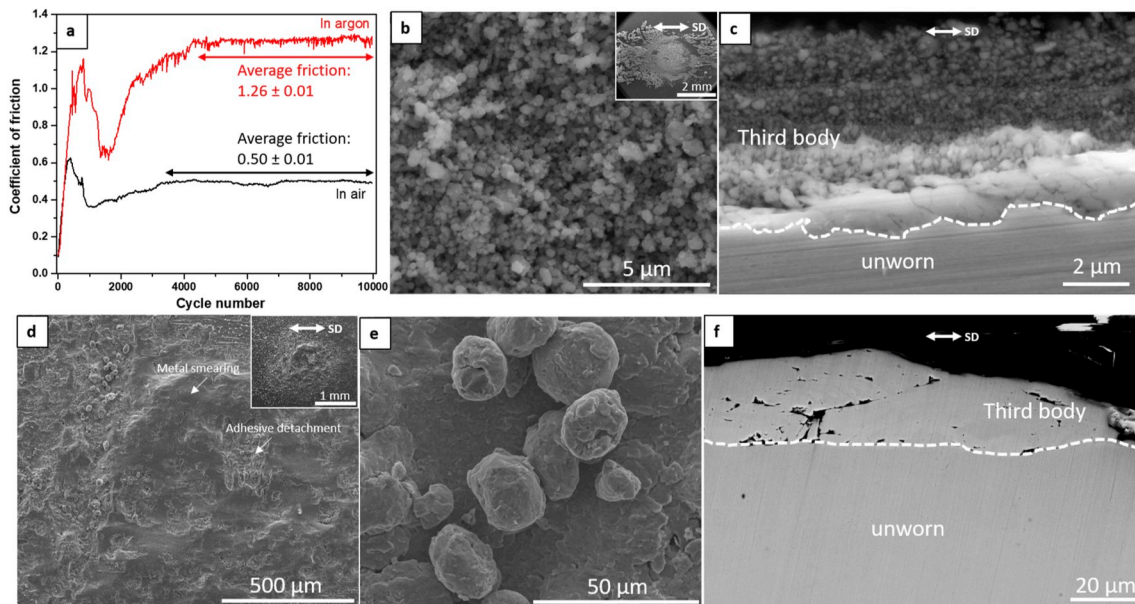


Fig. 14. (a) A plot of coefficients of friction vs. cycle number running in air and argon. (b) typical third body morphology of the wear track running in air, inset is a whole view of the wear scar; (c) cross sectional morphology of the third body layer. (d) plan view of the wear track running in argon, the inset shows the entire wear track; (e) morphology of agglomerates formed during sliding; (f) cross sectional morphology of the third bodies. SD indicates sliding direction.

When the simulation results are applied to interpret the present experiment, it is reasonable to assign the fretting in air to the linear friction regime, where with low cohesion, the third body particles behave in a manner of Couette flow or lamellar flow, resulting in low coefficient of friction; nevertheless, the test in argon can be explained using third body rheology observed in the high cohesion regime (5–20 GPa). The strong cohesion between metallic third body particles contributes to formation of the agglomerates, which are either compacted or rolling in the contact. Consequently, our simulations and experiments are consistent and support each other.

It's worth to note that the absolute friction values of experiments and simulations are not the same. One possible explanation is that the simulation represents a small portion of a sliding contact, which is at microscale; yet the experiments conducted here are at macroscale. Another possible reason is that even though the above experiments running in air and argon were assigned to the linear friction regime and the constant friction regime at high cohesion, respectively, numerous third body behaviours often occurred simultaneously in the real contact. Third, the limits of the current model discussed in Section 3.4 suggest the simulated friction here are more phenomenological quantity. Additional efforts are required to establish links to real tribological results. Therefore, it is not surprising that the absolute values from simulations and experiments are not identical.

4. Conclusions

In summary, a multibody meshfree model was successfully applied to examine third body rheology in a dry sliding contact; it revealed explicitly local third body dynamics and provided theoretical evidence of direct links between third body rheology and friction. The following conclusions can be drawn according to the present study:

1. Microscale coefficient of friction was governed by third body rheology, that varied with cohesion strength between third body particles. Three friction regimes were therefore observed: linear friction regime at low cohesion, transition friction regime at medium cohesion and constant friction regime at high cohesion.
2. In the linear friction regime, the friction increased linearly with cohesion. Third body rheology exhibited as Couette flow or lamellar flow, in which shearing between particles was the major velocity accommodation mode. In the transition friction regime, third body particles arranged as strong inclined force chains, and the velocity was adapted by rapid breakdown and regeneration of the force chains. In the constant friction regime, however, the third body particles were drastically deformed and agglomerated. Formation and rolling of the agglomerate led to reduction in friction.
3. For all friction regimes, shear force and normal force were transmitted by stress concentration chains that connected two first bodies. Therefore, load transfer often activated all the third body particles.
4. The activated third body thickness (ATT) to accommodate velocity gradient depended largely on third body rheology. In the transition and constant friction regimes, it followed the same trend as friction with cohesion increase; hence the coefficient of friction increased linearly with the ATT. This conclusion provides a possible novel method of material design to control the friction.

CRedit authorship contribution statement

Yinyin Zhang: Conceptualization, Methodology, Investigation, Writing - original draft. **Guilhem Mollon:** Supervision, Conceptualization, Writing - review & editing. **Sylvie Descartes:** Supervision, Conceptualization, Writing - review & editing, Funding acquisition.

Acknowledgements

The authors gratefully thank the agency of national research (ANR)

for financial support of the project (ANR-16-CE08-0016-X-FEW).

References

- [1] Gebeshuber IC. Ecotribology: development, prospects, and challenges. In: Ecotribology. Springer; 2016. p. 1–39.
- [2] Berthier Y, Vincent L, Godet M. Fretting fatigue and fretting wear. *Tribol Int* 1989; 22(4):235–42.
- [3] Singer I, Dvorak S, Wahl K, Scharf T. Role of third bodies in friction and wear of protective coatings. *J Vac Sci Technol A: Vac Surf Films* 2003;21(5):S232–40.
- [4] Godet M. The third-body approach: a mechanical view of wear. *Wear* 1984;100(1): 437–52.
- [5] Berthier Y. Third-body reality—consequences and use of the third-body concept to solve friction and wear problems. *Wear Mater Mech Pract* 2005:1.
- [6] Descartes S, Berthier Y. Rheology and flows of solid third bodies: background and application to an MoS₂ 6 coating. *Wear* 2002;252(7–8):546–56.
- [7] Strauss HW, Chromik RR, Hassani S, Klemberg-Sapieha JE. In situ tribology of nanocomposite Ti–Si–C–H coatings prepared by PE-CVD. *Wear* 2011;272(1): 133–48.
- [8] Chromik R, Strauss H, Scharf T. Materials phenomena revealed by in situ tribometry. *JOM* 2012;64(1):35–43.
- [9] Stoyanov P, Shockley JM, Dienwiebel M, Chromik RR. Combining in situ and online approaches to monitor interfacial processes in lubricated sliding contacts. *MRS Communications* 2016;6(3):301–8.
- [10] Manimunda P, Al-Azizi A, Kim SH, Chromik RR. Shear-induced structural changes and origin of ultralow friction of hydrogenated diamond-like carbon (DLC) in dry environment. *ACS Appl Mater Interfaces* 2017;9(19):16704–14.
- [11] Scharf T, Singer I. Role of the transfer film on the friction and wear of metal carbide reinforced amorphous carbon coatings during run-in. *Tribol Lett* 2009;36(1): 43–53.
- [12] Shockley JM, Descartes S, Irissou E, Legoux J-G, Chromik R. Third body behavior during dry sliding of cold-sprayed Al–Al₂O₃ composites: in situ tribometry and microanalysis. *Tribol Lett* 2014;54(2):191–206.
- [13] Iordanoff I, Berthier Y, Descartes S, Heshmat H. A review of recent approaches for modeling solid third bodies. *J Tribol* 2002;124(4):725–35.
- [14] Cundall PA, Strack OD. A discrete numerical model for granular assemblies. *Geotechnique* 1979;29(1):47–65.
- [15] Fillot N, Iordanoff I, Berthier Y. A granular dynamic model for the degradation of material. *J Tribol* 2004;126(3):606–14.
- [16] Fillot N, Iordanoff I, Berthier Y. Modelling third body flows with a discrete element method—a tool for understanding wear with adhesive particles. *Tribol Int* 2007;40 (6):973–81.
- [17] Haddad H, Guessasma M, Fortin J. A DEM–FEM coupling based approach simulating thermomechanical behaviour of frictional bodies with interface layer. *Int J Solids Struct* 2016;81:203–18.
- [18] Iordanoff I, Fillot N, Berthier Y. Numerical study of a thin layer of cohesive particles under plane shearing. *Powder Technol* 2005;159(1):46–54.
- [19] Iordanoff I, Seve B, Berthier Y. Solid third body analysis using a discrete approach: influence of adhesion and particle size on macroscopic properties. *J Tribol* 2002; 124(3):530–8.
- [20] Leonard BD, Ghosh A, Sadeghi F, Shinde S, Mittelbach M. Third body modeling in fretting using the combined finite-discrete element method. *Int J Solids Struct* 2014;51(6):1375–89.
- [21] Mollon G. A numerical framework for discrete modelling of friction and wear using Voronoi polyhedrons. *Tribol Int* 2015;90:343–55.
- [22] Cao H-P, Renouf M, Dubois F, Berthier Y. Coupling continuous and discontinuous descriptions to model first body deformation in third body flows. *J Tribol* 2011;133 (4):041601.
- [23] Shockley JM, Rauch EF, Chromik RR, Descartes S. TEM microanalysis of interfacial structures after dry sliding of cold sprayed Al–Al₂O₃. *Wear* 2017;376–377:1411–7.
- [24] Zhang Y, Choudhuri D, Scharf TW, Descartes S, Chromik RR. Tribologically induced nanolaminate in a cold-sprayed WC-reinforced Cu matrix composite: a key to high wear resistance. *Mater Des* 2019;182:108009.
- [25] Mollon G. A multibody meshfree strategy for the simulation of highly deformable granular materials. *Int J Numer Methods Eng* 2016;108(12):1477–97.
- [26] Mollon G. A unified numerical framework for rigid and compliant granular materials. *Comput Part Mech* 2018:1–11.
- [27] Mollon G. Solid flow regimes within dry sliding contacts. *Tribol Lett* 2019;67(4): 120.
- [28] Ren F, Bellon P, Averback RS. Nanoscale self-organization reaction in Cu–Ag alloys subjected to dry sliding and its impact on wear resistance. *Tribol Int* 2016;100: 420–9.
- [29] Zhang Y, Descartes S, Chromik RR. Influence of WC on third body behaviour during fretting of cold-sprayed CuMoS₂WC composites. *Tribol Int* 2019;134:15–25.
- [30] Zhang Y, Chromik RR. Tribology of self-lubricating metal matrix composites. In: Self-lubricating composites. Springer; 2017.
- [31] Chandross M, Grest GS, Stevens MJ. Friction between alkylsilane Monolayers: molecular simulation of ordered monolayers. *Langmuir* 2002;18(22):8392–9.
- [32] Zhao H, Barber G, Liu J. Friction and wear in high speed sliding with and without electrical current. *Wear* 2001;249(5–6):409–14.
- [33] Nayroles B, Touzot G, Villon P. Generalizing the finite element method: diffuse approximation and diffuse elements. *Comput Mech* 1992;10(5):307–18.
- [34] Mollon G. Mixtures of hard and soft grains: micromechanical behavior at large strains. *Granul Matter* 2018;20(3):39.

- [35] Berthier Y, Vincent L, Godet M. Velocity accommodation in fretting. *Wear* 1988; 125(1):25–38.
- [36] Baydoun S, Fouvry S, Descartes S, Arnaud P. Fretting wear rate evolution of a flat-on-flat low alloyed steel contact: a weighted friction energy formulation. *Wear* 2019;426–427:676–93.
- [37] Fouvry S, Kapsa P, Vincent L. Analysis of sliding behaviour for fretting loadings: determination of transition criteria. *Wear* 1995;185(1):35–46.
- [38] Bowden FP, Tabor D. The friction and lubrication of solids, 1. Oxford university press; 2001.
- [39] Zhang J, Majmudar T, Sperl M, Behringer R. Jamming for a 2D granular material. *Soft Matter* 2010;6(13):2982–91.
- [40] Bi D, Zhang J, Chakraborty B, Behringer RP. Jamming by shear. *Nature* 2011;480(7377):355–8.
- [41] Berthier Y. Experimental evidence for friction and wear modelling. *Wear* 1990;139(1):77–92.
- [42] Horgan CO, Saccomandi G. A molecular-statistical basis for the Gent constitutive model of rubber elasticity. *J Elast* 2002;68(1–3):167–76.
- [43] Zhang J, Majmudar T, Behringer R. Force chains in a two-dimensional granular pure shear experiment. *Chaos: Interdisciplin J Nonlinear Sci* 2008;18(4):041107.